Optimization of nanotube electrode geometry in a liquid crystal media from wavefront aberrations

Ranjith Rajasekharan, Qing Dai, Haider Butt, Kanghee Won, Timothy D. Wilkinson,* and Gehan A. J. Amaratunga

Department of Electrical Engineering, University of Cambridge, Cambridge, UK

*Corresponding author: tdw13@cam.ac.uk

Received 19 July 2011; revised 23 August 2011; accepted 23 August 2011; posted 24 August 2011 (Doc. ID 151145); published 24 January 2012

This paper presents experimental optimization of number and geometry of nanotube electrodes in a liquid crystal media from wavefront aberrations for realizing nanophotonic devices. The refractive-index gradient profiles from different nanotube geometries—arrays of one, three, four, and five—were studied along with wavefront aberrations using Zernike polynomials. The optimizations help the device to make application in the areas of voltage reconfigurable microlens arrays, high-resolution displays, wavefront sensors, holograms, and phase modulators.

OCIS codes: 230.0230, 230.3720, 350.4238, 350.4600.

1. Introduction

From the previous literature on the hybrid combination of carbon nanotubes and liquid crystals [1–11], it has been found that there is a strong interaction between them because of the large size difference between the liquid crystal molecules (1–2 nm) and carbon nanotubes (a few nanometers to micrometers). This interaction can be interpreted as an optical interaction through the optical anisotropy of the liquid crystal. Hence, vertically grown multiwall carbon nanotube (MWCNT) electrodes fabricated on silicon or quartz substrate and covered with a nematic liquid crystal can be used to form defect centers in the liquid crystal and then the liquid crystal can be manipulated by applying an external electric field [3]. The carbon nanotube electrode was fabricated using the plasma enhanced chemical vapor deposition technique and electron-beam lithography [3,9]. The nanotubes were patterned in small groups of one, three, four, and five with 1 μm spacing between nanotubes in each group and 10 μm spacing between the groups. We have done the computational optimization to study electric field profile from the nanotube electrodes using finite element method modeling in [8].

In this paper, we demonstrate optimization of carbon nanotube electrode number and geometry experimentally from wavefront aberrations in a nanophotonic device based on the hybrid combination of a sparse array of MWCNTs grown on a silicon surface and covered with nematic liquid crystals. The nanotube electrode geometry was varied in each group as one, three, four, and five, and the group was repeated in 10 μm separation. The refractive-index gradient profile was obtained from the phase profile at each nanotube site (photonic element) for different geometries. Then wavefront aberrations from these photonic elements were studied using Zernike polynomials. Based on the results from experiments, the electrode number and geometry was optimized mainly for high-resolution display and lens array applications.

2. Experimental Optimization of the Electrode Geometry

The scanning electron microscope (SEM) images of nanotube electrodes with different geometries and numbers are shown in Fig. 1. The height of the nanotube electrode was around 6 μm.

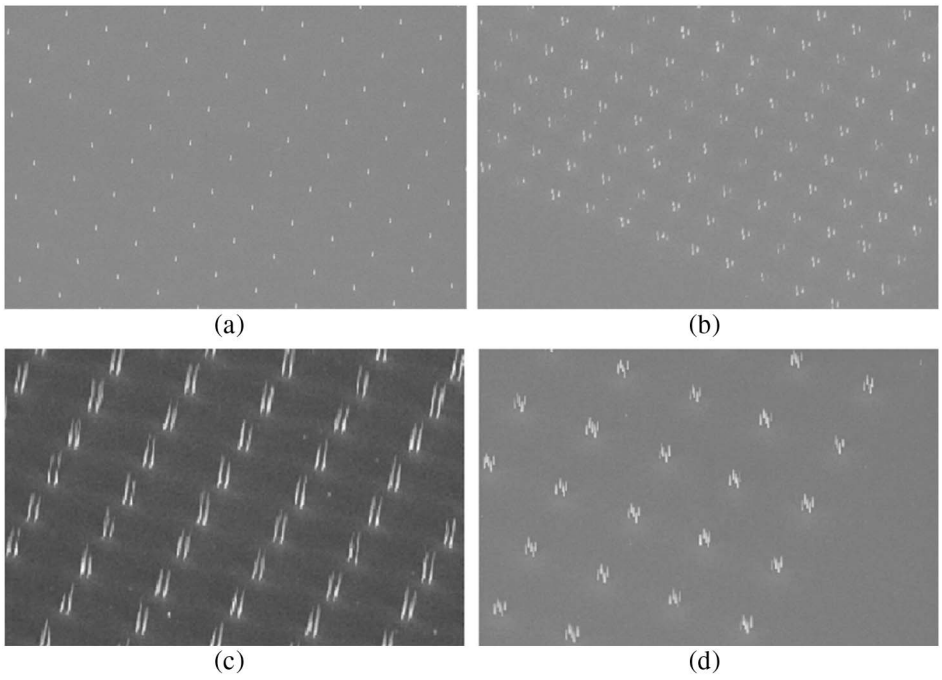

Fig. 1. SEM image of nanotube electrodes on silicon substrate, in groups of (a) one, (b) three, (c) four, and (d) five.

The sparse array was then fabricated into a liquid crystal device. In order to make the device reflective and to provide a common electrical connection to all the nanotubes, 400 nm of aluminum was cold sputtered onto the bottom substrate where the carbon nanotubes were grown. The sparse array was then assembled with a top electrode containing indium-tin oxide (ITO) on 0.7 mm thick borosilicate glass into a liquid crystal cell with a 20 μm cell gap set by spacer balls in the UV glue. There was no alignment layer for the liquid crystal on the nanotube array (bottom electrode), but the top glass electrode was coated with AM4276 (low pretilt polyimide from Merck) and rubbed in the horizontal direction to give planar alignment. The cell was then capillary filled with BL048, a positive dielectric anisotropy nematic liquid crystal mixture, also from Merck. The nanotubes act as individual electrode sites that spawn an electric field profile, dictating the refractive-index profile within the liquid crystal and, hence, creating a series of graded index profiles, which form voltage reconfigurable photonic elements. The electric field profile from the nanotube is approximately Gaussian in shape [5]. A Gaussian electric field profile may not generate a Gaussian refractive-index profile because the liquid crystal is nonlinear to the applied voltage [12]. In the current device, there is one more effect that deviates from the expected Gaussian index profile, which is that the planar alignment was given only on the top ITO substrate and, hence, nematic liquid crystals were aligned in hybrid fashion. Therefore, even though the electric field profile is Gaussian in shape, the liquid crystal molecules are finally oriented in a complex geometry because of nonlinearity combined with the surface effects of the alignment layer applied to the upper substrate of the cell and vertically grown nanotubes on bottom substrate. The result of these effects creates a varying refractive-index profile across the device that is a quasi-Gaussian under an applied voltage. The ideal refractive-index profile to minimize the wavefront aberration is a parabolic profile.

3. Microscopic Refractive-Index Profile

The microscopic phase profile and refractive-index gradient profile of each element around the nanotube was of interest as it decides the real modulation capability and applications of the device. In the reflective devices, the light has a double pass through the device. In this double pass, light is refracted through the liquid crystal, then reflected from the aluminum layer, and then again refracted through the liquid crystal. When the device was characterized under a polarized optical microscope, it was found that the light focuses by each lenslet at a particular voltage and focal length was voltage reconfigurable. The threshold voltage of the device was measured as 0.6 V rms, which corresponds to the Fréedericksz transition of BL048, and it was observed that, above 1 V rms, the nanotube arrays were all fully switched. The aperture size of each lenslet was found to increase with respect to the applied voltage up to a limiting size of 10 μm, and further increase in voltage distorted the refractive-index profile of the lenslets. This was further studied by using an interference setup attached to a reflective optical microscope. The setup was used to recover the interference fringes and, hence, the phase profile from each lenslet, and the recovered phase profile was used to understand how the device modulates a planar wavefront. The setup consisted of an He–Ne laser along with a beam expander as the illuminating source. A

microscopic objective having a magnification of ×20 was used in the microscope. The device was mounted on a fine three-axis tilting stage and attached to the microscope in reflective mode. The rubbing direction of the device was kept at 45° to the polarizer. The interference fringes were formed due to the interference between the ordinary and extraordinary beams being combined by an analyzer, which was crossed with the polarizer [12]. A rotating diffuser (transparent plastic sheet) was used to average out speckle noise. The fringes were captured by a CCD camera and a frame grabber. A white-light source was used to see the device and to help in the alignment. A voltage source was used to study the variation of interference fringes at different applied voltages.

The phase profile for each of the nanotube electrode geometry was recovered from the interference fringes to study refractive-index profile of the device. The unwrapped phase profile was recovered from the interference fringes using a modified Fourier transform technique [13]. The phase profile is found to be quasi-Gaussian in shape at a particular voltage and, hence, at the light focusing. The focal length of each lenslet was calculated using the equation $f = \frac{\Gamma^2}{2\mathrm{OPD}}$ [14,–16], where OPD is the peak-to-valley optical path difference from the center to the edge of the hybrid grating lenslet and Γ is the radius of the test area (5 μm). The focal length was 10 μm at 0 V rms and increased to 27 μm at 3 V rms. Further increase in the voltage distorted the orientation of liquid crystal molecules in the device and, hence, no focusing was observed.

The refractive-index variation or gradient across each lenslet was obtained from the unwrapped phase profile using the equation $\Delta n = \frac{\lambda \Delta\varphi}{4\pi d}$ [17], where Δn is the refractive-index variation, λ is the wavelength of light (633 nm), d is the thickness of the device (20 μm), and $\Delta\varphi$ is the unwrapped phase difference across the sample.

4. One-Nanotube Electrode Geometry

Figure 2 shows interference fringes recorded from the one-nanotube device at different applied voltages using the interference set up. It was found that fringes were observed at 0 V rms because the nanotube distorted the planar alignment of the liquid crystal molecules around it. The fringes were symmetric and wide at around 1.3 V rms. The fringes disappeared as the voltage increased above 3 V rms. This is because the liquid crystal molecules aligned almost homeotropically at higher voltages. Figure 2(d) shows the unwrapped phase profile of one lenslet. The unwrapped phase became symmetric and wider at around 1.3 V rms and distorted as the voltage increased. The maximum phase modulation observed was 4π. The refractive-index variation was obtained from the unwrapped phase profile, as shown in Fig. 2(e). The maximum variation between circumference to the center of the lenslet was 0.042. The refractive index varied continuously across the device. The refractive-index variation between the ordinary and extraordinary light was 0.2627. Around 17% of this variation (0.2627) was exploited in the device. The one-nanotube electrode geometry gives a symmetrical phase profile as well as refractive-index profile and is suitable for lens array applications. However, the field profile is narrow, which results in small diameter lenslets and, hence,

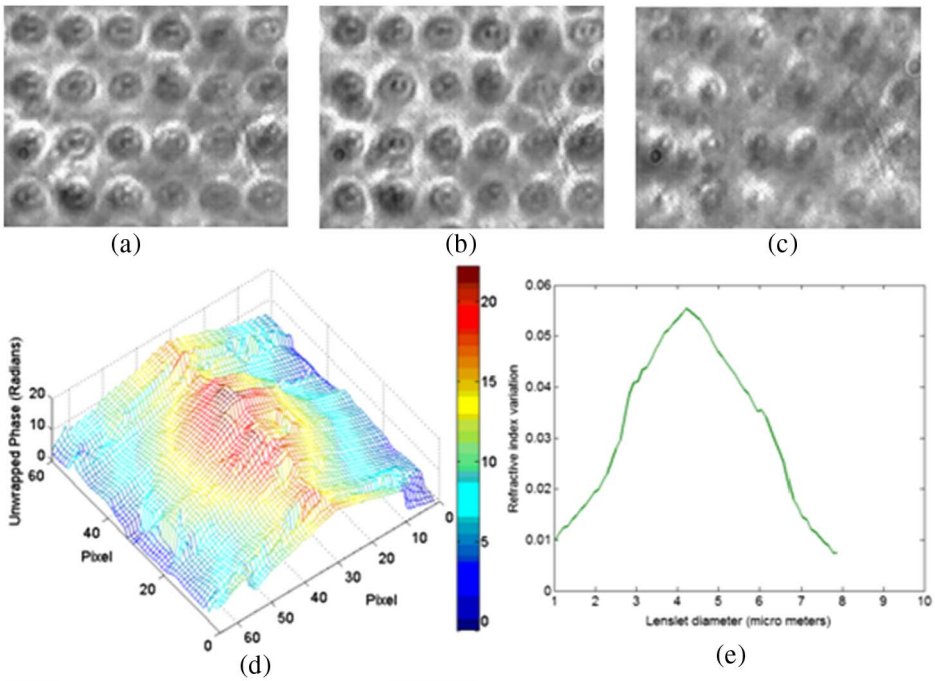

Fig. 2. (Color online) Interference fringes at different voltages from one-nanotube device: (a) 0 V rms, (b) 1.3 V rms, and (c) 3.5 V rms. (d) Unwrapped phase at 1.3 V rms (e) Refractive-index profile across one lenslet.

the lensing is weak. However, the single-nanotube electrodes are suitable for high-resolution display applications where each nanotube site acts as a pixel with minimum fringing field effects by applying suitable voltages.

5. Three-Nanotube Electrode Geometry

Figure 3 shows the interference fringes obtained from the three-nanotube pattern device. It was clear from the interferogram that the fringes were asymmetric and distorted. The unwrapped phase profile was recovered to understand the phase modulation and symmetry in detail. Figure 3(d) shows the unwrapped phase profile of a lenslet at 1.3 V rms. The lenslet diameter increased with voltage and there was more overlapping between lenslets at around 1.3 V rms The refractive-index variation was obtained from the unwrapped phase profile, as shown in Fig. 3(e). The maximum variation between circumference to the center of the lenslet was 0.034. The three-nanotube electrode was not best suited for lensing applications as th phase profile and refractive-index profile were distorted.

6. Four-Nanotube Electrode Geometry

Figure 4 shows interference fringes from the device at different applied voltages: 0, 1.3, and 3 V rms. The fringes were wider at around 1 V rms with maximum phase modulation capability. The fringes disappeared at higher voltages, as discussed for the previous geometries. Figure 4(d) shows the unwrapped phase profile of one lenslet. The unwrapped phase became almost symmetric and widest at around 1 V rms and distorted as the voltage increased. The refractive-index variation was obtained from the unwrapped phase profile, as shown in Fig. 4(e). The maximum refractive-index variation between circumference to the center of the lenslet was 0.044. The four-nanotube electrode geometry gave an almost symmetrical phase profile as well as a refractive-index profile with wide resultant field and was suitable for a lens array.

7. Five-Nanotube Electrode Device Geometry

Figure 5 shows interference fringes recovered from the device at different applied voltages. The fringes are almost symmetrical with a small distortion at the center of the fringes. This is because the center nanotube in the five group distorts the refractive-index profile at the center of each lenslet. This was further studied by recovering the unwrapped phase from the fringes. Figure 5(d) shows the unwrapped phase profile of one lenslet. The maximum refractive-index variation between circumference to the center of the lenslet was 0.04, as shown in Fig. 5(e). The lenslet phase profile and refractive-index profile were distorted mainly at the center of each lenslet. Although the fringes were almost symmetrical for the five-nanotube geometry, there was distortion at the center of each lenslet and it was not suitable for lens array applications.

8. Wavefront Aberrations

Zernike polynomials [18] were used to estimate aberrations of the wavefront from the phase profile generated by the devices with different nanotube geometries. Zernike polynomials are polynomials defined over a unit circle in radial coordinates (R and θ). They are favored for representing wavefronts because they are orthogonal within the unit circle in

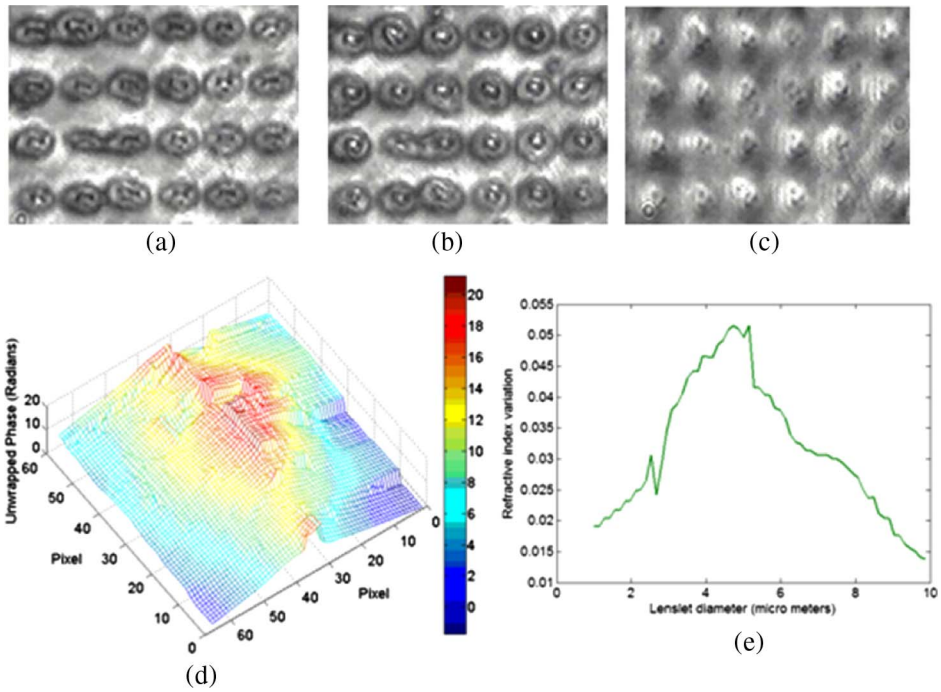

Fig. 3. (Color online) Interference fringes at different voltages from three-nanotube device: (a) 0 V rms, (b) 1.3 V rms, and (c) 3.5 V rms. (d) Unwrapped phase of a three-nanotube lenslet at 1.3 V rms. (e) Refractive-index profile across one lenslet.

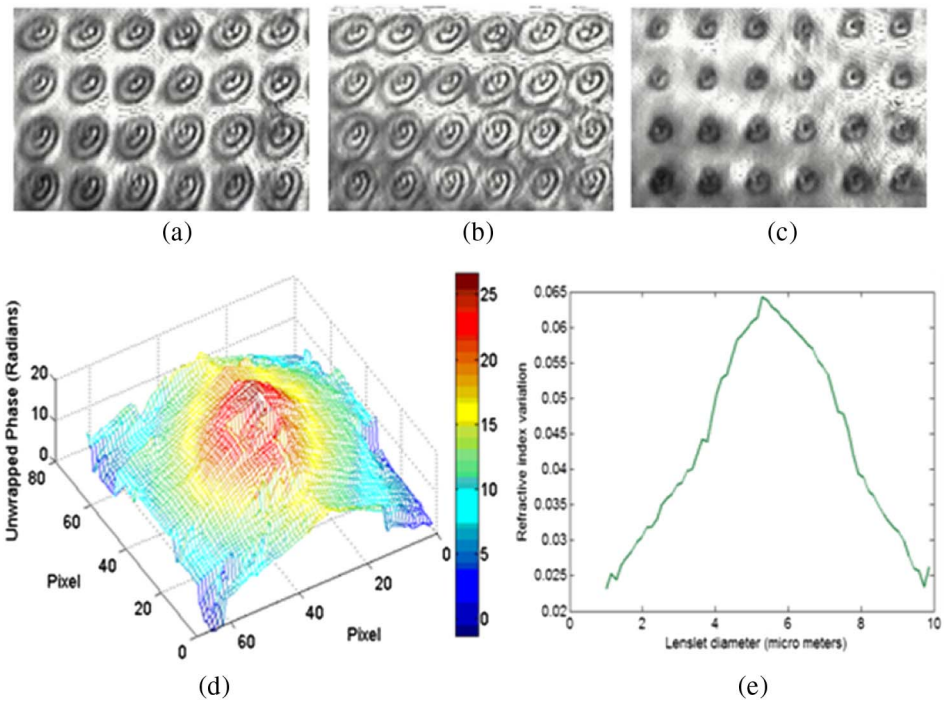

Fig. 4. (Color online) Interference fringes at different voltages from four-nanotube device: (a) 0 V rms, (b) 1.3 V rms, and (c) 3.5 V rms. (d) Unwrapped phase at 1.3 V rms (e) Refractive-index profile across one lenslet.

which they are defined. The polynomial is less reliable in regions outside the circle because measured data are fit inside the unit circle.

Figure 6 represents the wavefront aberrations from the nanotube electrode devices with nanotubes in groups of one, three, four, and five. The polynomials were identified from a standard chart (fringe Zernike polynomials). The first four mode numbers (Z_0^0, Z_1^{-1}, Z_1^1, and Z_2^0) have not been taken into account for any comparison here because these mode numbers give only piston, tilt in the x axis, tilt in the y axis, and defocus. Figure 6(a) shows first 15 Zernike aberration coefficients for the one-nanotube device. The primary astigmatism $Z_2^{-2}(+)$ and spherical aberration $Z_4^0(+)$ were prominent here compared to other aberrations. The first 15 Zernike coefficients for the three-nanotube electrode device are shown in Fig. 6(b). The major aberrations were primary

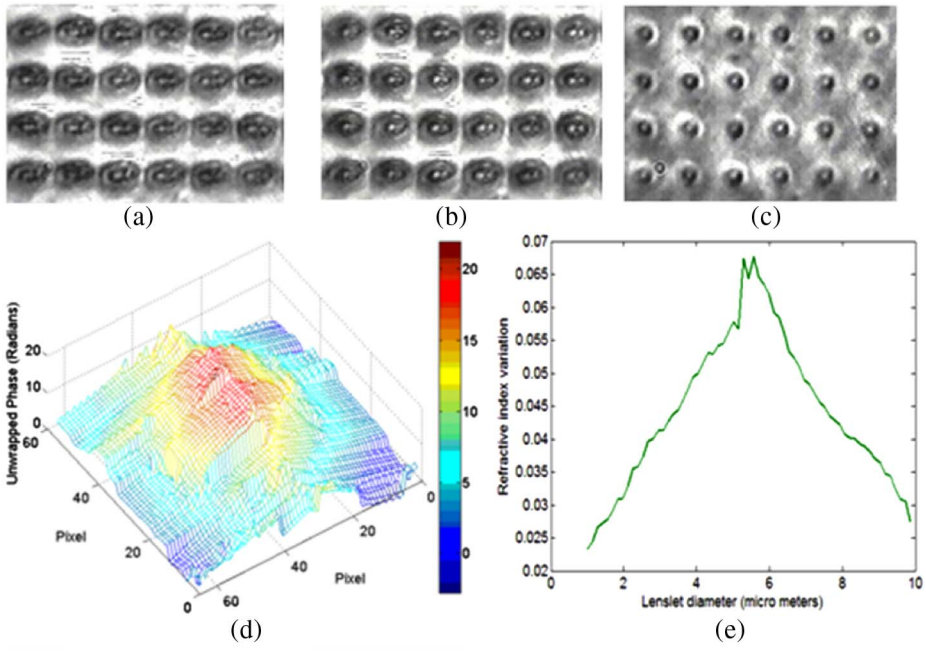

Fig. 5. (Color online) Interference fringes at different voltages from the five-nanotube device: (a) 0 V rms, (b) 1.3 V rms, and (c) 3.5 V rms. (d) Unwrapped phase at 1.3 V rms. (e) Refractive-index profile across one lenslet.

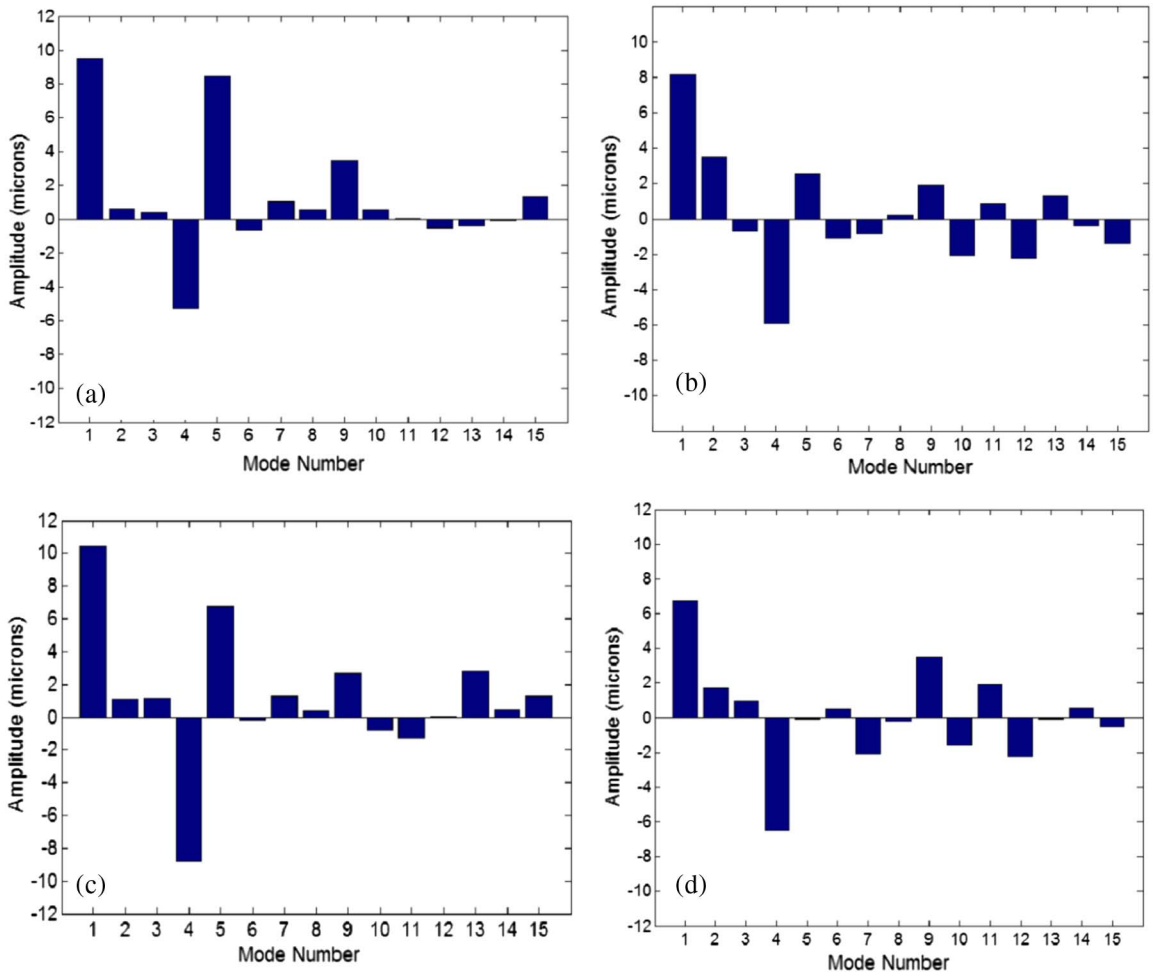

Fig. 6. (Color online) Spectra of Zernike coefficients for (a) one, (b) three, (c) four, and (d) five-nanotube devices.

astigmatism $Z_2^{-2}(+)$, spherical aberration $Z_4^0(+)$, primary trefoil $Z_3^{-3}(-)$, and secondary astigmatism (axis at 0° or 90°) $Z_4^{-2}(-)$. This is because the three-nanotube electrode group spawned an asymmetrical electrical field at each lenslet position.

Figure 6(c) represents the first 15 Zernike coefficients for the four-nanotube electrode device. The major aberrations were primary astigmatism $Z_2^{-2}(+)$, spherical aberration $Z_4^0(+)$, and secondary astigmatism (axis at ±45°) $Z_4^{-2}(+)$. The overall aberration was more than the single-nanotube device but less than the three-nanotube device. Figure 6(d) represents the first 15 Zernike coefficients for the five-nanotube electrode device. The major aberrations were primary coma (x axis) $Z_3^{-1}(-)$, spherical aberration $Z_4^0(+)$, primary trefoil (y axis) $Z_3^3(+)$, and secondary astigmatism (axis at 0° or 90°) $Z_4^{-2}(+)$. From the wavefront aberrations it was clear that the one-nanotube geometry was found to be suitable for high-resolution display applications where each nanotube site can act as a single pixel. This geometry gave a small lenslet diameter for lens array applications and, hence, formed a weak lens array. The three-nanotube geometry considerably distorted the wavefront and, hence, was not suitable for either display or lens array applications. The four-nanotube device geometry was suitable for lens array applications, but not the five-nanotube device because the middle nanotube electrode distorted the wavefront at the center of the nanotube group. The four-nanotube geometry also can be used for pixel design in display applications with reduced separation between each nanotube in the group. We have also calculated Zernike modes for the devices. We have also observed changes in the modes with respect to the voltage. However, the current result is limited by the accuracy of the phase unwrapping technique used and Zernike approximation. Although the Zernike approximation is effective for describing the individual lower- and higher-order aberrations, it also has a smoothing effect that can significantly limit the aberrations that account for the wavefront error. Because of limitations with Zernike (modal) reconstruction, a different reconstruction method, such as zonal reconstruction, can be considered for improving the accuracy.

9. Conclusions

Carbon nanotube electrode number and geometry was optimized in a liquid crystal media for realizing

nanophotonic devices for high-resolution display and lens array applications. The nanotubes were grown on silicon substrate and then sealed with nematic liquid crystal using glass coated with ITO to make a nanophotonic device. When an electric field is applied between nanotube electrodes and the top ITO coated glass, the electric field aligned the liquid crystal molecules and created a gradient refractive-index profile across the device. Devices with different numbers and geometries were fabricated. The refractive-index profile and wavefront aberrations at each nanotube site were obtained for the detailed study. The one-nanotube geometry with overall less wavefront aberration was found to be suitable for high-resolution display applications where each nanotube site can act as a single pixel. This geometry gave a small lenslet diameter for lens array applications and, hence, formed a weak lens array. The three-nanotube geometry distorted the refractive-index profile and, hence, was not suitable for either display or lens array applications. The four-nanotube device geometry was suitable for lens array applications, but not the five-nanotube device because the middle nanotube electrode distorted the refractive-index profile and, hence, the wavefront at the center of the nanotube group. The four-nanotube geometry also can be used for pixel design in display applications with reduced separation between nanotubes in the group. Higher numbers of nanotubes per group were also considered, such as six and eight. The six-nanotube geometry is also suitable for microlens array applications with a wider lenslet aperture. The nanotube electrodes can form a closed circle with a different diameter, without any electrode at the center (like the center electrode in the five-nanotube group) or inside the closed circle for lens array applications. This is because the inside electrode distorts the refractive-index profile of the lenslet formed. However, as the number of nanotubes increased, there were more phase aberrations. So a trade-off between number of nanotubes per group and the aperture of each lenslet is required, depending upon the application.

The authors thank Samsung Electronics Co., Ltd. (SAIT) for funding this work. Thanks also to Stephen Morris, Flynn Castles, Philip Hands, and Damian Gardner for fruitful discussions.

References

1. S.-Y. Lu and L.-C. Chien, "Carbon nanotube doped liquid crystal OCB cells: physical and electro-optical properties," Opt. Express **16**, 12777–12785 (2008).
2. S. J. Jeong, P. Sureshkumar, K.-U. Jeong, A. K. Srivastava, S. H. Lee, S. H. Jeong, Y. H. Lee, R. Lu, and S.-T. Wu, "Unusual double four-lobe textures generated by the motion of carbon nanotubes in a nematic liquid crystal," Opt. Express **15**, 11698–11705 (2007).
3. T. D. Wilkinson, X. Wang, K. B. K. Teo, and W. I. Milne, "Sparse multiwall carbon nanotube electrode arrays for liquid-crystal photonic devices," Adv. Mater. **20**, 363–366 (2008).
4. R. Rajasekharan, Q. Dai, and T. D. Wilkinson, "Electro-optic characteristics of a transparent nanophotonic device based on carbon nanotubes and liquid crystals," Appl. Opt. **49**, 2099–2104 (2010).
5. W. I. Milne, K. B. K. Teo, M. Chhowalla, G. A. J. Amaratunga, S. B. Lee, D. G. Hasko, H. Ahmed, O. Groening, P. Legagneux, L. Gangloff, J. P. Schnell, G. Pirio, D. Pribat, M. Castignolles, A. Loiseau, V. Semet, and V. Thien Binh, "Electrical and field emission investigation of individual carbon nanotubes from plasma enhanced chemical vapour deposition," Diamond Rel. Mater. **12**, 422–428 (2003).
6. R. Rajasekharan, H. Butt, and T. D. Wilkinson, "Optical phase modulation using a hybrid carbon nanotube-liquid crystal nanophotonic device," Opt. Lett. **34**, 1237–1239 (2009).
7. R. Rajasekharan, C. Bay, Q. Dai, J. Freeman, and T. D. Wilkinson, " Electrically reconfigurable nanophotonic hybrid grating lens array," Appl. Phys. Lett. **96**, 233108 (2010).
8. H. Butt, R. Rajasekharan, T. D. Wilkinson, and G. A. J. Amaratunga, "Electromagnetic modeling of multiwalled carbon nanotubes as nano-rod electrodes for optimizing device geometry in a nanophotonic device," IEEE Trans. Nanotechnol. **10**, 547–554 (2010).
9. Q. Dai, R. Rajesekharan, H. Butt, K. Won, X. Wang, T. D. Wilkinson, and G. Amaratunga, "Transparent liquid crystal based microlens array using vertically aligned carbon nanofibre electrodes on quartz substrates," Nanotechnology **22**, 115201 (2011).
10. X. Wang, T. D. Wilkinson, M. Mann, K. B. K. Teo, and W. I. Milne, "Characterization of a liquid crystal microlens array using multiwalled carbon nanotube electrodes," Appl. Opt. **49**, 3311–3315 (2010).
11. R. Rajesekharan, T. D. Wilkinson, P. J. W. Hands, and Q. Dai, "Nanophotonic three-dimensional microscope," Nano Lett. **11**, 2770–2773 (2011).
12. S.-T. Wu, U. Efron, and L. D. Hess, "Birefringence measurements of liquid crystals," Appl. Opt. **23**, 3911–3915 (1984).
13. R. Rajesekharan, C. Bay, J. Freeman, and T. D. Wilkinson, "Analysis of an array of micro lenses using Fourier-transform method," IET Optoelectron. **4**, 210–215 (2010).
14. H. Ren and S. T. Wu, "Liquid crystal lens with large focal length tunability and low operating voltage," Opt. Express **15**, 11328—11335 (2007).
15. H. Ren, Y. H. Fan, and S. T. Wu, "Tunable electronic lens using a gradient polymer network liquid crystal," Appl. Phys. Lett. **82**, 22–24 (2003).
16. A. K. Kirby, P. J. Hands, and G. D. Love, "Liquid crystal multimode lenses and axicons based on electronic phase shift control," Opt. Express **15**, 13496–13501 (2007).
17. R. Escalona, "Study of axial absorption in liquids by interferometry," J. Opt. A **5**, S355 (2003).
18. M. Born and E. Wolf, *Principles of Optics*, 6th ed. (Pergamon, 1980).